

## Intermetallic Compounds

# Chemical Behaviour of CaAg<sub>2</sub> under Ethylene Epoxidation Conditions

Iryna Antonyshyn,<sup>\*[a]</sup> Olga Sichevych,<sup>[a]</sup> Karsten Rasim,<sup>[a]</sup> Alim Ormeci,<sup>[a]</sup> Ulrich Burkhardt,<sup>[a]</sup> Sven Titlbach,<sup>[b]</sup> Stephan Andreas Schunk,<sup>[b]</sup> Marc Armbrüster,<sup>[c]</sup> and Yuri Grin<sup>\*[a]</sup>

**Abstract:** The binary compound CaAg<sub>2</sub> is examined as a catalyst for the ethylene epoxidation reaction. During the induction phase, conversion and selectivity increase and then remain stable for several hundred hours. The presence of ethyl chloride as a promoter is crucial. The pristine CaAg<sub>2</sub> reacts with the gase-

ous reactants and forms a porous microstructure of calcium-containing oxidation products on the surface, in which particles of elemental silver are embedded. The microstructure is remarkably stable, and in particular, prevents further sintering of the silver particles.

## Introduction

Silver is a unique catalyst for two industrially relevant processes: ethylene epoxidation and partial oxidation of methanol to formaldehyde.<sup>[1]</sup> Nevertheless, the selectivity towards the target product ethylene oxide (EO) in the epoxidation reaction amounts to only 40–50 % for unpromoted silver catalysts<sup>[2]</sup> and can be improved to about 85–90 % by using a variety of promoters, which are typically used in technical processes.<sup>[1,3]</sup> Aiming for a rational understanding and/or design of alternative catalysts, a deep insight into the underlying reactions and the dynamic changes of the catalyst material is decisive. Consequently, the last decades have seen enormous efforts in studies using both experimental techniques and computational methods. The “hot” topics are adsorption of oxygen onto Ag,<sup>[1,4]</sup> the nature of the active species<sup>[1,4c–4e]</sup> and reaction intermediates,<sup>[5]</sup> the mechanism of ethylene epoxidation,<sup>[1,6]</sup> the role of the support,<sup>[1,7]</sup> promoters<sup>[1,8]</sup> and size effects.<sup>[1,9]</sup>

Still debated in detail, there are two fundamentally different approaches for the discussion of the ethylene epoxidation reaction: (i) the consideration of different types of oxygen species and their roles in the ethylene epoxidation;<sup>[1,4,10]</sup> and (ii) the “oxametallacycle” model,<sup>[1,6]</sup> which largely relies on suitable oxygen species from model (i). Nowadays, intense research is focused on the nature of electrophilic oxygen species, theoretical predictions and experimental proofs of reaction intermed-

ates (e.g., oxametallacycle OMC), optimization of catalyst particle size, the development of suitable supports and the search for new synthesis routes for catalysts.<sup>[11–16]</sup>

Based on a variety of studies of the epoxidation reaction, it is evident that the electronic structure of the surface layer of the catalyst has a tremendous influence on the adsorption properties of reactants and the occurrence of specific reaction intermediates. Depending on the adsorption strength of reactants and intermediates, as well as desorption rates of reaction products, the rate-determining step can vary, largely governing reaction pathways, and therefore, overall selectivity. Bimetallic catalysts have been assumed to be useful systems for tuning the catalytic activity by modifying the electronic structure. DFT calculations on simplified models, where individual Ag atoms on the surface are replaced by atoms of another metal, predict catalytic performance for Ag–Cu, Ag–Au and Ag–Pd catalysts.<sup>[17]</sup> The enhancement of the selectivity towards ethylene oxide for supported Ag–Cu and Ag–Pd bimetallic catalysts, compared with elemental Ag, has also been experimentally confirmed.<sup>[17,18]</sup> However, advanced investigations of Ag–Cu catalysts under reaction conditions reveal no metallic or alloyed copper on the surface of these catalysts. Instead, thin oxide-like “CuO” layers are detected and the mechanism of ethylene epoxidation turns out to be strongly surface-structure dependent.<sup>[19]</sup> There seems to be no unique surface structure that is responsible for the catalytic activity. The chemistry of the Ag–Cu catalyst system is highly dynamic and not trivial. The complexity of such catalytic systems sometimes also leads to discrepancies between theoretical calculations and experimental evidence. For example, the Ag–Cd catalyst is unselective towards ethylene oxide, according to density functional theory (DFT) calculations,<sup>[20]</sup> whereas experimental studies have shown enhanced selectivity, compared with elemental Ag.<sup>[21]</sup> This can be explained by oversimplified assumptions in the model for the calculation: the oxidizing conditions of ethylene epoxidation dramatically change the oxidation states of the surface atoms, and thus, their adsorption properties. In the same direc-

[a] Max-Planck-Institut für Chemische Physik fester Stoffe,  
Nöthnitzer Str. 40, 01187 Dresden, Germany  
E-mail: Iryna.Antonyshyn@cpfs.mpg.de  
Grin@cpfs.mpg.de  
[http://www.cpfs.mpg.de/chemical\\_metal\\_science](http://www.cpfs.mpg.de/chemical_metal_science)

[b] hte GmbH,  
Kurfalzring 104, 69123 Heidelberg, Germany

[c] Technische Universität Chemnitz, Fakultät für Naturwissenschaften,  
Institut für Chemie,  
Straße der Nationen 62, 09111 Chemnitz, Germany

 Supporting information and ORCID(s) from the author(s) for this article are available on the WWW under <https://doi.org/10.1002/ejic.201800710>.

tion, is the finding that zinc oxide ZnO segregates to the surface during kinetic studies of supported Ag-Zn catalysts.<sup>[22]</sup>

The need for further understanding of the oxygen incorporation into silver-based catalysts is the reason to investigate CaAg<sub>2</sub>, one of the binary compounds in the Ca-Ag system with ordered crystal structure. The crystal structure of intermetallic compounds (IMCs), as the consequence of their chemical bonding, makes them useful model systems for understanding the behaviour of catalysts under reaction conditions. This has been well documented for hydrogenation reactions.<sup>[23]</sup> Here, a combined experimental and computational study on the CaAg<sub>2</sub> compound under ethylene epoxidation conditions is presented.

## Results and Discussion

### Characterization of As-Prepared Samples

Single-phase samples of CaAg<sub>2</sub> were synthesized using the heat treatment described in the Experimental Section. The obtained samples were well crystallized (Figure 1, top) and brittle. They are stable in an argon atmosphere at room temperature and oxidize slowly during exposure to air.

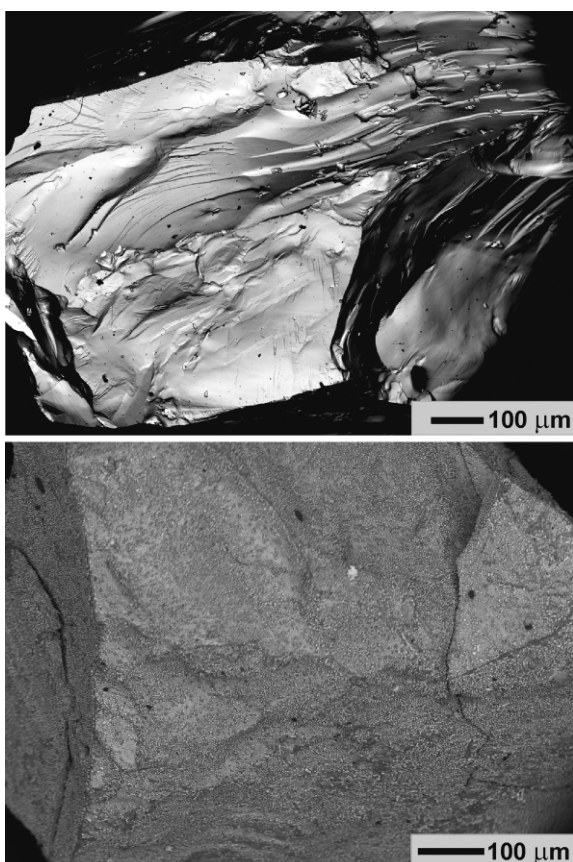


Figure 1. Morphology of CaAg<sub>2</sub> particles (BSE detector, 8 kV, material contrast): (top) as-prepared and (bottom) after catalytic test.

The binary compound CaAg<sub>2</sub> crystallizes with the KHg<sub>2</sub>-type crystal structure (space group *Imma*).<sup>[24]</sup> Figure 2 (top) presents the results of the crystal structure refinement of CaAg<sub>2</sub> from powder X-ray diffraction data. Indexing of the reflections from

the X-ray powder diffraction pattern (PXRD), recorded using internal standard LaB<sub>6</sub>, and subsequent refinement yield lattice parameters  $a = 4.691(1)$  Å,  $b = 7.295(2)$  Å,  $c = 8.135(1)$  Å, which are in perfect agreement with literature data [ $a = 4.689(1)$  Å,  $b = 7.301(2)$  Å,  $c = 8.139(3)$  Å].<sup>[24]</sup> The summarized information is shown in Table S1 and confirms the KHg<sub>2</sub>-type of crystal structure. In the "zig-zag" chains along [100] ( $d_1 = 2.731$  Å, orange in Figure 2, bottom), the Ag atoms are interconnected, forming planar honeycomb-like nets. The interatomic distances Ag-Ag between these chains are slightly longer  $d_2 = 2.772$  Å (green in Figure 2, bottom). The planar nets are interlinked to a three-dimensional (3D) framework by longer bonds of  $d_3 = 2.900$  Å along [010]. The calcium atoms are located in the cavities of this framework. Because of the orthorhombic deformation of the pristine hexagonal AlB<sub>2</sub>-type structure, the trigonal prisms around the silver atoms are strongly deformed and the coordination number of Ag becomes 10 (6 × Ca plus 4 × Ag).

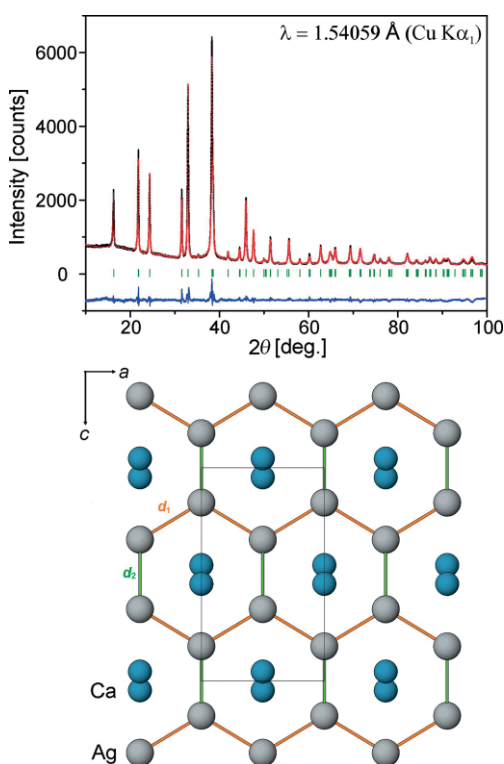


Figure 2. (top) Experimental (black), calculated (red), and difference (blue) powder X-ray diffraction patterns of CaAg<sub>2</sub> (peak positions are shown in green). (bottom) View of the crystal structure of CaAg<sub>2</sub> along [010].

The single-phase nature of the synthesized samples is additionally confirmed using differential thermal analysis (DTA, Figure S1). One only sharp endothermic peak, at 600 °C, on heating, corresponds to the decomposition of CaAg<sub>2</sub>, following the peritectic reaction  $\text{CaAg}_2 \rightarrow \text{Ca}_2\text{Ag}_7 + L$ , which is in good agreement with literature data of 596 °C<sup>[25a]</sup> and 597 °C,<sup>[25b,25c]</sup> respectively.

These results reveal that CaAg<sub>2</sub> samples can be synthesized reproducibly, with sufficient composition and structural control, using the described synthesis route.

## Catalytic Measurements

Ethylene epoxidation using  $\text{CaAg}_2$  as the catalyst was performed, varying temperature ( $T$ ), gas hourly space velocity (GHSV), and amount of ethyl chloride (EC) in the gas stream (Figure 3). The selectivity towards ethylene oxide increases and reaches 60–65 % in about 30 h, whereas the conversion level remains relatively low during the whole experiment and does not exceed 1.5–2.5 %. The observed increase of selectivity at the beginning indicates the presence of an induction period during which the catalyst is transformed to its active state. Usually, the existence of an induction period reflects a noticeable modification; for example, the formation of an oxygen-containing layer in oxidative catalysis.<sup>[26]</sup> As expected, a positive impact on the conversion is observed at lower GHSV values ( $1000 \text{ h}^{-1}$ ), because of the longer contact time of the reaction mixture with the catalyst (Figure 3).

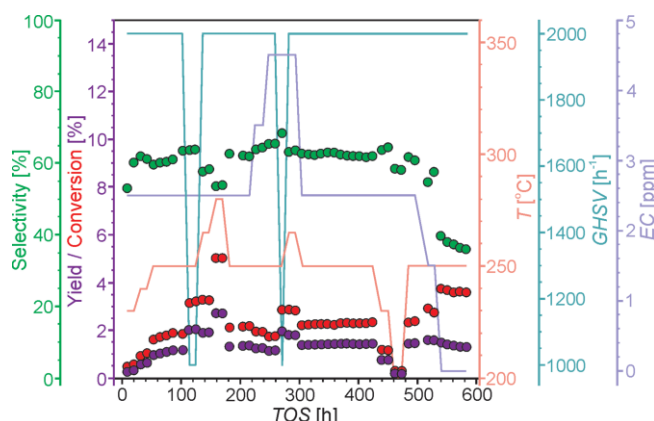


Figure 3. Ethylene epoxidation on  $\text{CaAg}_2$ : conversion of ethylene (red), yield of EO (violet) and selectivity towards EO (green) as a function of time on stream (TOS). Variation of experimental conditions ( $T$ , GHSV, amount of EC) are shown with solid lines.

An increase in the conversion is achieved at elevated temperatures (up to  $280^\circ\text{C}$ ), but simultaneously, a significant drop of selectivity is observed. Even a slight increase of temperature by  $30^\circ\text{C}$  reduces the selectivity from 64 to 53 %. The same trends of conversion and selectivity dependence on the reaction temperature are known for different types of silver catalysts: sponge-like,<sup>[27]</sup> powder,<sup>[28]</sup>  $\text{Ag}(111)$  single crystals,<sup>[29]</sup>  $\text{Ag}/\alpha\text{-Al}_2\text{O}_3$ <sup>[30]</sup> etc.

The reduction of the EC concentration, and finally, its absence in the reactive gas stream leads to a significant drop of selectivity from 64 to 34 % (Figure 3). Thus, the presence of the ethyl chloride promoter is crucial for the catalytic performance.

## Post-Catalytic Characterization of $\text{CaAg}_2$

The surface morphologies of the particles before and after exposure to reaction conditions are completely different (Figure 1). Elemental mapping of as-synthesized sample shows a homogeneous distribution of Ca and Ag within the particles, but the presence of a tiny oxygen signal should also be mentioned.

After the catalytic test ( $T_{\max} = 280^\circ\text{C}$ ,  $\text{GHSV} = 1000\text{--}2000 \text{ h}^{-1}$ ,  $0\text{--}4.5 \text{ ppm EC}$ ), the whole surface of the  $\text{CaAg}_2$  crumbs is covered by small particles (Figure 1, bottom). Elemental mapping and energy-dispersive X-ray spectroscopy (EDXS) at different points and regions (Figure 4) shows the presence of elemental Ag agglomerates (ca.  $1\text{--}3 \mu\text{m}$  in size) on the surface (point 1), areas with different Ca/Ag ratios (points 2–3) and oxygen enrichment of calcium-rich regions (point 3). The corresponding spectra are presented in Figure S2. The more detailed determination of the compositions for the Ca-Ag phases is hampered by the presence of oxygen and the roughness of the surface.

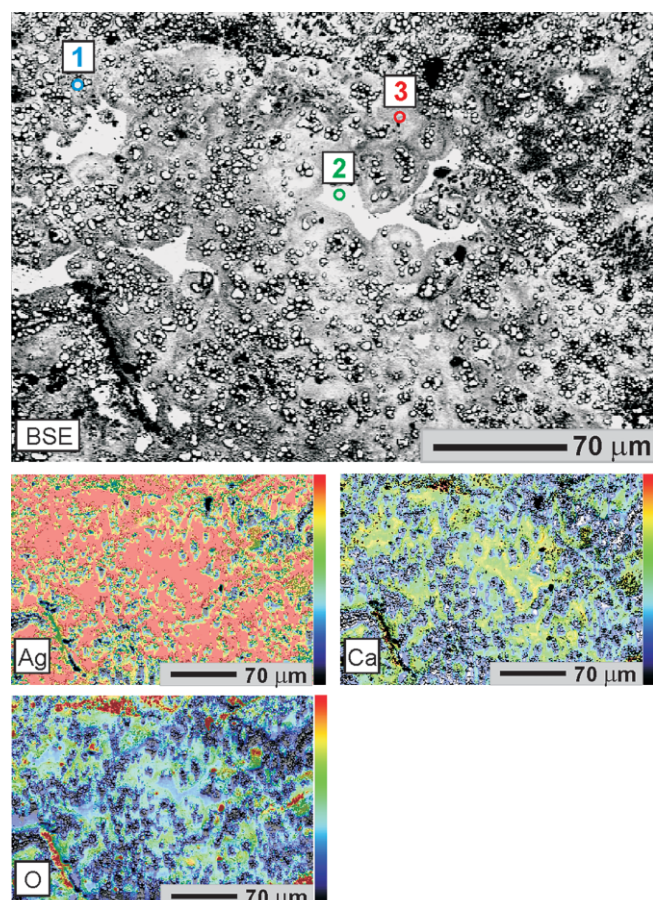


Figure 4.  $\text{CaAg}_2$  particle after catalytic test (BSE detector, 8 kV, material contrast): (top) morphology of the surface; and (bottom) elemental mapping (colour-coded intensity distribution).

SEM results are in agreement with powder X-ray diffraction data (Figure 5), which evidences the presence of  $\text{CaAg}_2$ ,  $\text{Ca}_2\text{Ag}_7$ , and elemental Ag under reaction conditions. Calcium-related oxidation products are not clearly identified by PXRD, most probably due to their small amount and low degree of crystallinity.

In general, the oxidation of  $\text{CaAg}_2$  under ethylene epoxidation conditions can be schematically described as in Scheme 1. As the calcium-containing product of the  $\text{CaAg}_2$  oxidation,  $\text{CaO}$  was assumed, but due to the presence of carbon dioxide and water vapour in the gas stream (products of the undesired full oxidation of ethylene  $\text{C}_2\text{H}_4 + 3\text{O}_2 \rightarrow 2\text{CO}_2 + 2\text{H}_2\text{O}$ ), as well

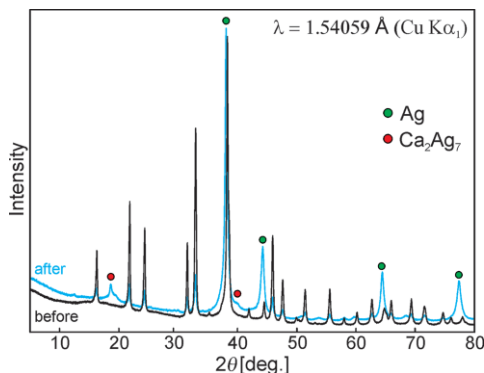
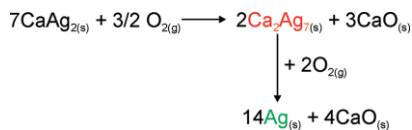


Figure 5. X-ray diffraction patterns of the  $\text{CaAg}_2$  sample before (black) and after (blue) the ethylene epoxidation experiment (600 h on stream, non-marked reflections correspond to  $\text{CaAg}_2$ ).

as ethyl chloride (as the promoter), the formation of calcium hydroxide  $\text{Ca}(\text{OH})_2$ , carbonate  $\text{CaCO}_3$ , as well as chloride  $\text{CaCl}_2$ , cannot be excluded.



Scheme 1. Oxidation of  $\text{CaAg}_2$ .

The amount of  $\text{CaAg}_2$  decreases significantly after prolonged exposure to the gas stream, but even after 600 h it remains the majority phase, as inferred from the PXRD data.

Catalytic tests at elevated temperatures (up to 350 °C) lead to full oxidation of  $\text{CaAg}_2$  to elemental Ag and a mixture of  $\text{CaCO}_3$ ,  $\text{Ca}(\text{OH})_2$  and  $\text{CaO}$ ; the corresponding reflections are identified in PXRD patterns (Figure S3). This reveals that the formation of calcium-related products as result of  $\text{CaAg}_2$  oxidation is dynamic and depends on the amount and accessibility of water vapour and carbon dioxide on the surface of the catalyst. The catalytic performance of the obtained catalyst resembles one after a standard catalytic test ( $T_{\max} = 280$  °C) over 600 h ( $S = 65\%$ , conversion of ethylene: 1–3 %).

The short induction phase for  $\text{CaAg}_2$  in the ethylene epoxidation experiment (Figure 3), as well as the appearance of small Ag particles on the surface, reveal the in situ formation of Ag on a  $\text{CaO}/\text{Ca}(\text{OH})_2/\text{CaCO}_3$  support, to which catalytic activity and selectivity can be assigned. The formation of elemental Ag under reaction conditions is also supported by the fact that the selectivity is strongly dependent on the presence of ethyl chloride, as the promoter, in the gas stream (Figure 3). The promotion effect of Cl is a well-described feature of elemental Ag catalysts in ethylene epoxidation.<sup>[8a,8b,8f,31]</sup> This means that under ethylene epoxidation reaction,  $\text{CaAg}_2$  acts as a precursor for the formation of an elemental Ag catalyst. Nevertheless, the “stepwise” formed Ag catalyst ( $\text{CaAg}_2 \rightarrow \text{Ca}_2\text{Ag}_7 \rightarrow \text{Ag}$ ) is clearly more selective towards ethylene oxide than Ag nanoparticles supported on  $\text{CaO}$ , which were synthesized for comparison using classical impregnation techniques (Figure 6). Parallel formation of Ag particles and the calcium-containing support yield a 3D microstructure in the subsurface region. The latter ensures

the enhanced selectivity towards ethylene oxide and prevents the sintering of Ag particles, which is the main reason for the deactivation of industrially used Ag catalysts.<sup>[30b,32]</sup>

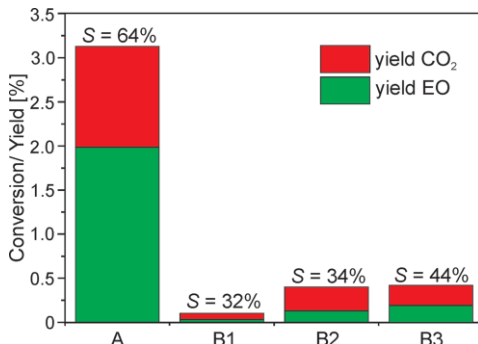


Figure 6. Ethylene epoxidation for different types of catalysts: conversion of ethylene (total height of the bars) and yields of EO/ $\text{CO}_2$  (coloured sections of the bars) ( $T = 250$  °C, 2.5 ppm EC) on A –  $\text{CaAg}_2$  ( $TOS = 114$  h), B1–5 wt.-%  $\text{Ag@CaO}$  ( $TOS = 192$  h), B2–15 wt.-%  $\text{Ag@CaO}$  ( $TOS = 192$  h), B3–30 wt.-%  $\text{Ag@CaO}$  ( $TOS = 192$  h)). Selectivity values ( $S$ ) are written on top of each bar graph.

## Electronic Structure and Chemical Bonding

The crystal structure was fully optimized. The obtained lattice parameters are  $a = 4.733$  Å,  $b = 7.339$  Å,  $c = 8.256$  Å, giving a 2.9 % larger unit cell volume, compared with the experimental values (cf. Characterization of As-Prepared Samples). The optimized atomic coordinates,  $z_{\text{Ca}} = 0.5446$ ,  $y_{\text{Ag}} = 0.0495$ ,  $z_{\text{Ag}} = 0.1623$ , are in good agreement with the experimental values (Table S1).

In the crystal structure of  $\text{CaAg}_2$ , each silver atom has four Ag near neighbours (distances  $2 \times d_1$ ,  $d_2$  and  $d_3$ ). In comparison with the elemental fcc Ag with 12 nearest neighbours, this number of Ag–Ag contacts in  $\text{CaAg}_2$  is rather small. Therefore, the implied decrease in d-d hybridization is expected to reduce the band width of the Ag (4d) states. Indeed, the Ag d band width of 2.5 eV in  $\text{CaAg}_2$  is smaller than 3.7 eV in fcc Ag (Figure 7, top). The top edge of the 4d band is located at -3.25 eV, and the centre of gravity at -4.49 eV. The corresponding values for the elemental Ag are -4.32 and -2.7 eV, respectively.

The (100) surface has the lowest surface energy (see below: Surface Energy Calculations). This surface has the same composition as the bulk; therefore, the behaviour of the Ag d DOS in the surface region is similar to that of the bulk. In a four-layer slab model, the subsurface Ag already closely resembles Ag in bulk  $\text{CaAg}_2$  (Figure 7, bottom). The bandwidth and centre of gravity values of subsurface Ag (4d) states are 2.5 and -4.53 eV, respectively, essentially identical to the corresponding bulk values. The d states of the top-layer Ag atoms shift to higher energies, the centre of gravity is at -4.21 eV, and since these Ag atoms are missing one of their  $d_1$  neighbours, the band width gets narrower, 2.35 eV. However, the top edge of the d bands remains the same in both bulk and surface.

The chemical bonding in an intermetallic compound is an essential component of the overall assessment of that compound's suitability for heterogeneous catalysis.<sup>[23c]</sup> The behaviour of IMC in the presence of various species under reaction

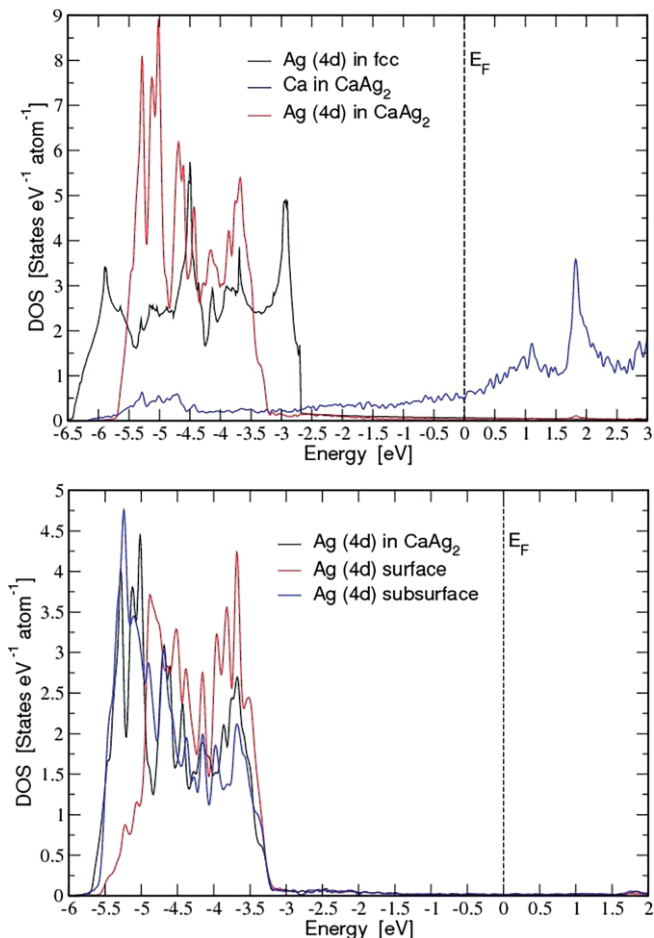


Figure 7. Electronic structure of  $\text{CaAg}_2$ : (top) Ca and Ag (4d) states for the optimized structure compared to the Ag (4d) DOS in fcc Ag; (bottom) comparison of Ag (4d) DOS in bulk, top and subsurface for the (100) surface.

conditions can be understood by analysing the atomic interactions.<sup>[23c]</sup> To have a better understanding of the chemical behaviour of  $\text{CaAg}_2$ , the electronic structural calculations were combined with a real-space study of the chemical bonding. The topological analysis of the electron density (ED) within QTAIM<sup>[33]</sup> reveals that a Ca atom loses 1.3 electrons so that each Ag atom gains 0.65 electrons. Hence, Ag becomes more nucleophilic than in the elemental solid. The shapes of the Ca and Ag QTAIM basins are very different (Figure 8, top). The Ca QTAIM basin is close to spherical, implying cationic character (ionic bonding). The boundaries between two Ag QTAIM basins are flat, indicating the covalent character of the interaction, while those between the Ag and Ca ones are round, as if cut from a sphere, characteristic of polar (ionic) interactions.

This finding already emphasizes a large ionic contribution to the Ca–Ag bonding. Further insight is obtained from an analysis of the electron localizability indicator (ELI-D). The spatial distribution of ELI-D in  $\text{CaAg}_2$  reveals only two types of attractors in the vicinity of the Ag–Ag contacts  $d_1$  and  $d_2$  (Figure 8, middle). The population of the bond basin  $b_1$  (0.5 electrons) is formed by two silver atoms separated by  $d_1$  (90 %) and by two neighbouring Ca atoms (10 %). The bond basin  $b_2$  contains 1.8 electrons: 1.2 of these originate from the silver atoms separated by

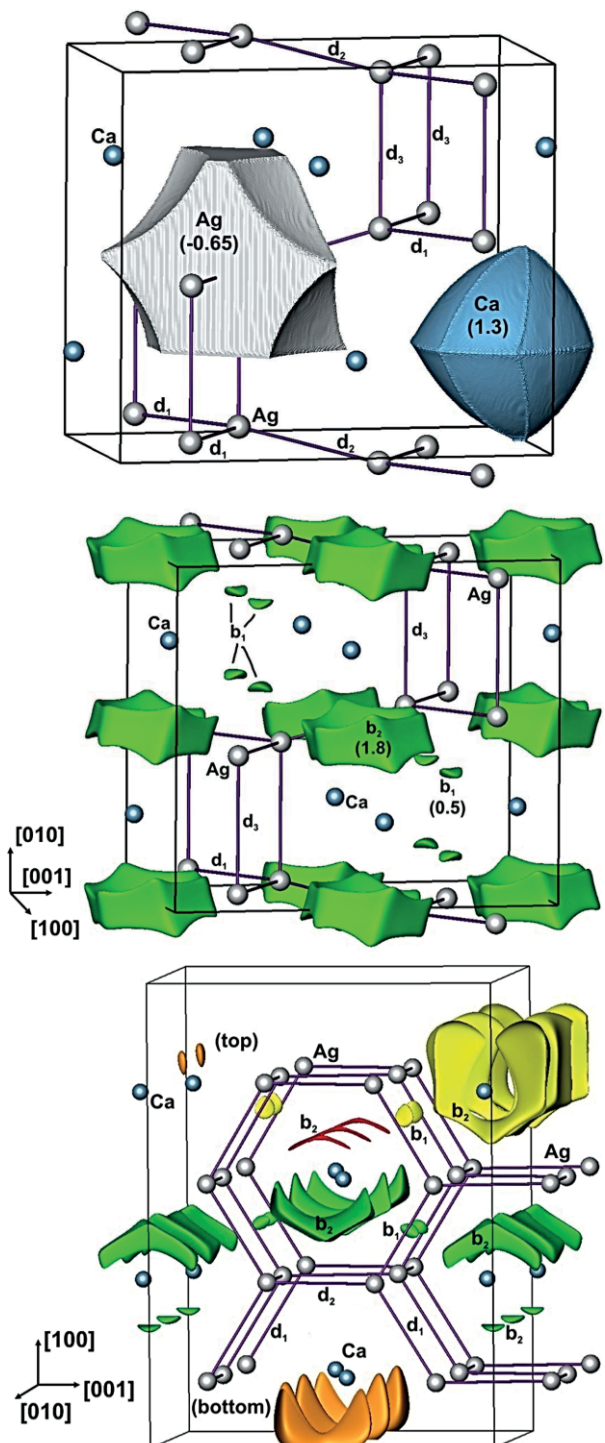


Figure 8. Chemical bonding in  $\text{CaAg}_2$ : (top) the Ag and Ca QTAIM basins with their effective charges; (middle) the ELI-D distribution in the  $\text{CaAg}_2$  unit cell with the three shortest Ag–Ag distances  $d_1$ ,  $d_2$ ,  $d_3$ ; isosurface value is 0.93,  $b_1$  and  $b_2$  stand for the bonds, the four Ag atoms contributing to the  $b_2$  bond are identified; (bottom) the ELI-D distribution for the four-layer slab model of the (100) surface for  $\text{CaAg}_2$ : the orange isosurface value is 1.045, the surface represents the dangling bonds; the yellow isosurface value is 0.954, the surface shows the localization domain of the combined dangling,  $b_2$  and the  $b_1$  bonds; the green isosurface value is 0.938, the surface shows the  $b_1$ - and  $b_2$ -like bonds in the inner region of the slab; the red isosurface value is 0.931, the surface depicts the  $b_2$ -type bond formed by the surface and subsurface Ag atoms. The black lines show the unit cell (top and middle) and calculated part of the structure (bottom).

$d_2$  (0.6 electrons each), another 0.44 are contributed by two Ag atoms with the  $d_1$  distance to the latter two, and the remaining 10 % is coming from two Ca atoms. Thus, both –  $b_1$  and  $b_2$  – mainly reflect the covalent interactions between two and four Ag atoms, respectively. These attractors reveal a formation of covalently bonded puckered anionic silver layers perpendicular to [010]. The calcium cations are embedded in between.

The ELI-D distribution was also computed for the four-layer slab model of the (100) surface (Figure 8, bottom). The Ag atoms in the top and bottom layers have one of their  $d_1$  neighbours missing; therefore, the according dangling bonds protruding into the vacuum region can be observed on both sides of the slab. The bonding features inside the slab correspond to bulk features in a very similar manner. The effective charges of the surface atoms do not deviate significantly from the corresponding bulk values. This finding suggests the scenario that when a species much more electronegative than Ag is introduced to the pristine surface, Ca atoms may prefer to form ionic bonds with that species, abandoning the Ag atoms. This may then result in the aggregation of Ag atoms.

### Surface Energy Calculations

The three principal directions [100], [010] and [001] were chosen for construction of possible surface termination in  $\text{CaAg}_2$  (Figure 9).

In the two latter cases, the crystal structure allows for different surface terminations. To obtain the surface energy of one surface structure only, the upper and lower sides of the simulation slabs have to be symmetric. However, this requirement leads to nonstoichiometric (with respect to the 2:1 Ag/Ca ratio) slabs for the cases (010)-I and (001)-III. The individual surface energies of these nonstoichiometric surfaces (Figure 10) thus depend on the chemical potential of the two components, which is limited by the heat of formation of the bulk compound. In this sense, a low-lying nonstoichiometric surface energy, such as the calcium-rich one for (010)-I, indicates a tendency to transform Ag-rich surfaces after cleaving into the calcium-terminated variant by Ag-precipitation, for example, upon annealing. The most favourable cleavage energies occur for flat surface terminations (variants I). In general, one observes almost identical values of the most favourable surface energies for different terminations, implying the equivalent ability to cleave in all directions. Furthermore, relaxation of the pristine surfaces only changes the surface energies to a negligibly small degree.

In view of the epoxidation reaction, the character of the surfaces under oxidizing conditions is of particular importance. A number of fully relaxed oxygen adsorption configurations was calculated. All results are related to dioxygen at the GGA-PBE level of theory. Given the electropositive character of the calcium, extremely large adsorption energies are observed for all configurations. Depending on the particular local environment, the energy gain varies between 2 and 4.6 eV per oxygen atom. Adsorption onto Ag (111), in comparison, yields merely a gain of 0.45 eV. A favourable local adsorption energy correlates with the number of locally available Ca atoms. Oxygen atoms occu-

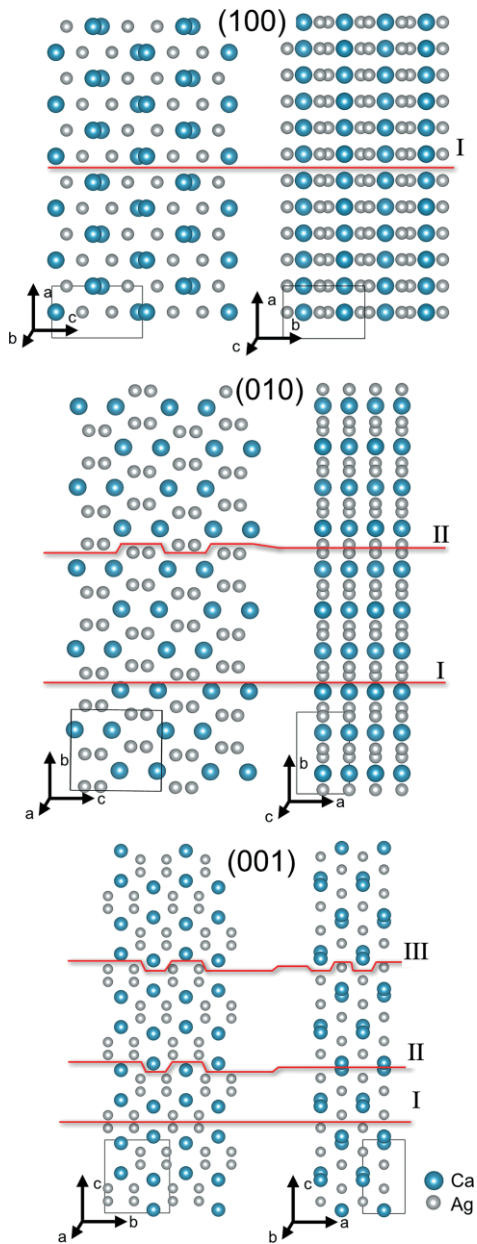


Figure 9. Cleavage of the crystal structure of  $\text{CaAg}_2$  and formation of possible terminating surfaces in different crystallographic directions.

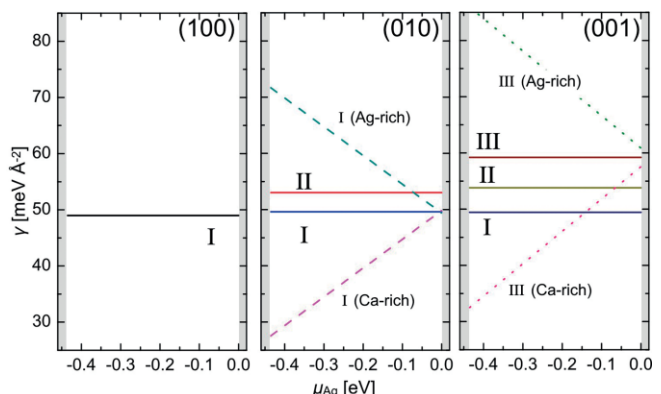


Figure 10. Surface energies of the terminating surfaces in  $\text{CaAg}_2$  (unrelaxed).

pying the centres of Ca tetrahedra or Ca triangles show the highest local adsorption energy. Such large adsorption energies will therefore provide a sizeable driving force for the transformation of the intermetallic compound to silver and CaO.

A more realistic view on this matter is given by an “ab initio thermodynamics approach”.<sup>[34]</sup> It relates adsorption energies, computed by DFT, to the partial pressure,  $p$ , of a gas species ( $O_2$  in this case) through the expression:

$$\gamma_{\text{ads}} (\text{meV \AA}^{-2}) = \frac{N_{\text{ox}}}{A} (E_{\text{ads}} - \Delta\mu(T, p_{\text{O}_2}))$$

where  $\gamma_{\text{ads}}$  is the adsorption energy per surface area,  $N_{\text{ox}}$  is the number of oxygen atoms adsorbed onto the surface area A of the slab and  $E_{\text{ads}}$  is the adsorption energy per oxygen atom with respect to the oxygen molecule.  $\mu$  is tabulated and accounts for the entropy difference between the  $\text{O}_2$  molecules in the gas phase and the immobile oxygen atoms at the surface. The values are taken from the NIST-JANAF thermochemical tables.<sup>[35]</sup> Each line in Figure 11 (top) corresponds to a particular calculated adsorption state characterized by the number of adsorbed oxygen atoms  $N_{\text{ox}}$  and their local configuration.

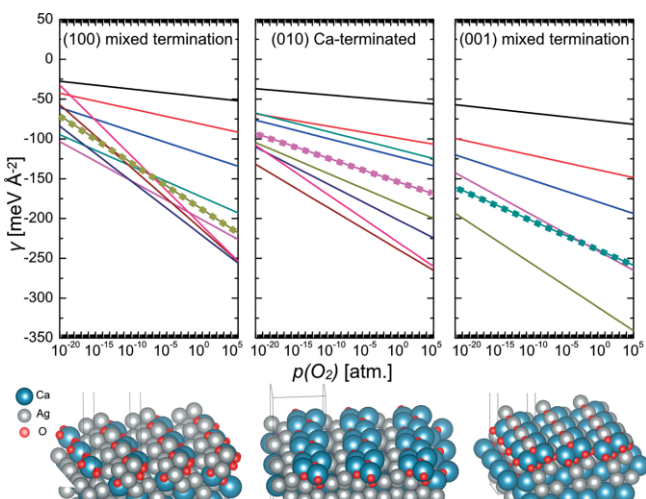


Figure 11. (top) Adsorption energies per surface area at 600 K of oxygen atoms (wrt. O<sub>2</sub>) on the most stable pristine surfaces (cf. Figure 10) of CaAg<sub>2</sub>. Lines with increasing slope correspond to an increasing oxygen coverage ( $N_{ox}$ ). Dashed lines indicate structures with full surface coverage and no subsurface oxygen atoms. (bottom) Structure of typical oxygenated surface configurations for (100), (010) and (001) facets (from left to right).

Configurations with the highest density of oxygen atoms, by definition, have the steepest negative slope with increasing oxygen partial pressure. The different absolute values thus correspond to the particular geometrical arrangements that can be more or less favourable. Representative high-coverage surface configurations are shown in Figure 11 (bottom).

The comparable degree of stabilization for each surface termination allows the conclusion that  $\text{CaAg}_2$  particles react in a similar manner in all directions, in agreement with experimental data (Figure 1, bottom). The corrosion process can proceed unhindered, as the resulting structures are quite open and allow easy access of the gas phase to the subsurface regions to

oxidize deeper-lying calcium atoms: the simple addition of more and more oxygen atoms *above* the already oxygen-covered surface slabs leads to oxygen migration (during the DFT relaxation; hence, without a kinetic barrier) towards the subsurface regions. The configurations of the lowest energy (Figure 11, bottom) already contain oxygen atoms beneath the surface. The indicated dashed lines correspond to the “last” surface structure that accommodates oxygen atoms exclusively at the surface, by which the region of the first atomic layer, in a geometrical sense, is meant. Concomitantly, with inwards oxygen migration, one observes the expulsion of silver out of the quite small surface unit cell. Any given Ca atom tends to optimize its oxygen coordination. A prime example is shown for the (100) termination, in which 3-atomic silver clusters form.

The experimental and theoretical results above clearly indicate a pronounced instability of the  $\text{CaAg}_2$  surfaces against reaction with oxygen under epoxidation conditions, which is governed by the extremely strong driving force towards the formation of calcium oxide. Potentially passivating layers that would qualify as energetically stable and geometrically dense were not found. On the one hand, this instability is consequently coupled to a segregation of silver atoms. On the other hand, similar oxidation in different crystallographic directions may produce a 3D microstructure of oxidation products on the surface, which may limit the size of the Ag particles, and thus, it ensures the stability of the catalytic system over a long time under the reaction conditions (Figure 12). Therefore, one may consider the intermetallic compound  $\text{CaAg}_2$ , under epoxidation conditions, to be a model precursor for Ag-based catalysts.

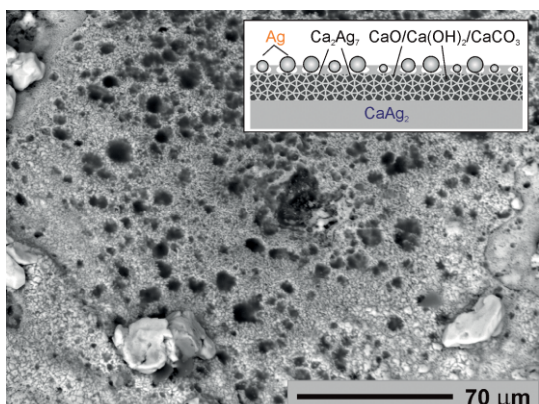


Figure 12. Microstructure of  $\text{CaAg}_2$  particle after ethylene epoxidation experiment with a porous 3D layer of  $\text{CaO}/\text{Ca}(\text{OH})_2/\text{CaCO}_3$  with particles of elemental Ag. Inset: schematic representation of the particle cross section.

## Conclusion

$\text{CaAg}_2$  was tested as a catalyst for ethylene epoxidation. The presence of more electronegative oxygen in the gas stream and the high affinity of the calcium to oxygen lead to the formation of calcium oxide and a substantial segregation of elemental silver to the surface. In addition to oxygen, carbon dioxide and water vapour from the undesired total combustion are in contact with the surface of the  $\text{CaAg}_2$ , leading to a variety of possible calcium-containing products of  $\text{CaAg}_2$  oxidation; for example

ple, CaO, Ca(OH)<sub>2</sub> and CaCO<sub>3</sub>. PXRD and SEM analysis of CaAg<sub>2</sub> particles after the catalytic test, as well as calculations of adsorption energies of oxygen atoms at different partial pressures, have confirmed the expulsion of Ag towards the surface and the formation of a 3D microstructure, which hinders further bulk oxidation of CaAg<sub>2</sub>. The latter can be only achieved at higher temperatures (up to 350 °C). The continuous dynamics of the Ag particles, which are homogeneously distributed in the CaO/Ca(OH)<sub>2</sub>/CaCO<sub>3</sub> 3D support, prevents their sintering and provides uniform values of selectivity towards ethylene oxide during almost 600 h of experiment. The comparison of CaO/Ca(OH)<sub>2</sub>/CaCO<sub>3</sub>-supported Ag catalyst (the product of CaAg<sub>2</sub> oxidation) with an Ag/CaO catalyst (prepared using a classical impregnation method) reveals the unique catalytic behaviour of the Ag-based catalyst obtained using CaAg<sub>2</sub> as a precursor.

## Experimental Section

Taking into account the high vapour pressure and chemical reactivity of calcium, all preparation steps were carried out in argon-filled glove boxes. Silver shot (1–6 mm, Alfa Aesar, 99.999 %) and dendritic calcium pieces (Alfa Aesar, 99.98 %) were weighed in a molar ratio of 2:1 and placed into tantalum containers, which were sealed under argon. The latter were placed into quartz glass ampoules and sealed under vacuum. The initial reaction was carried out in a resistance furnace by heating up to 1000 °C, dwelling at this temperature for 1 h, cooling down to 570 °C and subsequent annealing at this temperature for 340 h. After the above-mentioned heat treatment, the samples were quenched in ice water by breaking the quartz glass.

Supported Ag nanoparticles were prepared by incipient wetness impregnation of the CaO support (Sigma Aldrich) with an aqueous solution of silver nitrate (AgNO<sub>3</sub>), followed by drying ( $T = 80$  °C) and calcination ( $T = 280$  °C). The silver loadings were 5, 15 and 30 wt.-%.

Powder X-ray diffraction (PXRD) patterns were recorded with a Huber Imaging Plate Guinier Camera G670 (Cu-K<sub>α1</sub> radiation,  $\lambda = 1.54059$  Å), with lanthanum hexaboride LaB<sub>6</sub> ( $a = 4.1569$  Å) as the internal standard. The phase analysis, through the comparison of experimental and calculated PXRD patterns, was performed using WinXPow software.<sup>[36]</sup> For peak position determination, indexing of the powder X-ray diffraction patterns and the Rietveld refinement of the crystal structure, the WinCSD package<sup>[37]</sup> was employed.

Differential thermal analysis/thermogravimetry (DTA/TG) measurements under Ar flow were done with a Netzsch STA 449 C Jupiter F1 apparatus, situated in an Ar-filled box. The heating up to 650 °C and subsequent cooling to room temperature, with a rate of 10 °C/min, were carried out using tantalum crucibles without caps.

Scanning electron microscopy (SEM) using a JEOL 7800 electron microscope, with an attached EDX/EBSD system [Quantax 400, Bruker, Silicon-Drift-Detector (SDD), acceleration voltages 0.1 kV–30 kV], was utilized for several purposes: (i) checking the initial sample quality; (ii) determination of the composition of the synthesized compound; (iii) elemental mapping of the sample before and after the catalytic test; and (iv) morphology imaging of the sample surface after its exposure to reaction conditions. All preparation steps for SEM investigation were carried out in an Ar atmosphere and a dedicated shuttle-transfer system was used for sample insertion into the microscope. The samples were cold fixed in silver-containing epoxy resin or directly mounted on graphite tabs with-

out embedding (the latter was used in case of morphology studies). SiC papers and diamond powder with grain sizes of 3 µm or smaller were used for surface polishing.

Catalytic tests were performed using crushed bulk samples (ca. 1 cm<sup>3</sup>) sieved to a fraction with particle sizes of 500–1000 µm. The catalyst was filled between two layers of α-Al<sub>2</sub>O<sub>3</sub> (Alodur WSK F60, 250–315 µm) inside the tubular stainless-steel reactor (R0139). Pre-conditioning was carried out by heating to 160 °C (rate 1 °C/min) under nitrogen flow and dwelling at this temperature for 15 h. Further heating to 230 °C was accompanied with a switch from nitrogen to the reaction mixture [ethylene (35 vol. %), oxygen (7 vol. %), argon (5 vol. %; internal standard) and nitrogen (53 vol. %; carrier gas)]. As the promoter, ethyl chloride (EC) was added in a controlled way to the gas mixture. Different experiments, varying the temperature (230–350 °C), gas hourly space velocity (GHSV = 1000–2000 h<sup>-1</sup>) and amount of ethyl chloride (0–4.5 ppm), were performed. All tests were carried out at ambient pressure. Gas product analysis was done with gas chromatography (GC) and mass spectrometry (MS), analogously to procedures published elsewhere.<sup>[38]</sup>

The Fritz-Haber Institute ab initio molecular simulations package (FHI-aims)<sup>[39]</sup> was employed for investigating the electronic structure and chemical bonding features, geometry optimizations and surface calculations. The FHI-aims is an all electron, full-potential electronic structure code that employs atom-centred numerical basis functions. Exchange-correlation effects were taken into account within the generalized gradient approximation (GGA) to the density functional theory, as parametrized by Perdew–Burke–Ernzerhof (PBE).<sup>[40]</sup> The scalar relativistic effects were included by using a zeroth-order regular approximation (ZORA) approach.<sup>[41]</sup>

Chemical bonding analysis in position space was performed within the electron localizability approach, combining topological analysis of electron density (ED), based on the quantum theory of atoms in molecules (QTAIM)<sup>[33]</sup> and electron localizability indicator (ELI). ELI<sup>[42]</sup> was calculated in the ELI-D representation<sup>[43]</sup> by an own code using an interface to the FHI-aims.<sup>[44]</sup> Topological analysis of the ED and the ELI-D was carried out by the program DGrid.<sup>[45]</sup>

All surface energy and adsorption calculations were carried out using the slab approach within FHI-aims. The slabs contained at least five atomic layers, with a vacuum region of approximately 20 Å. Surface unit cells (1 × 1) of the (100), (010) and (001) orientations (8.26 × 7.33, 4.73 × 8.26, or 4.73 × 7.34 Å<sup>2</sup>) were used throughout. These dimensions correspond to the optimized bulk lattice parameters (GGA-PBE). In the case of one-sided, thus asymmetrical, adsorption configurations, a dipole-field correction, as implemented in FHI-aims, was employed. Surface energies and all adsorption energies were calculated by relaxing the adsorbate and all atoms of the top three surface layers.

## Acknowledgments

The authors are thankful to P. Scheppan and M. Eckert for SEM measurements, S. Scharsach and M. Schmidt for thermal analysis, and S. Hückmann for X-ray diffraction experiments.

**Keywords:** Intermetallic phases · Heterogeneous catalysis · Epoxidation · Chemical bonding · Adsorption energy

[1] V. I. Bukhtiyarov, A. Knop-Gericke, "Chapter 9: Ethylene Epoxidation over Silver Catalysts" in *Nanostructured Catalysts: Selective Oxidations* (Eds.: C. Hess, R. Schlögl), RSC Publishing, 2011, pp. 214–247, and references therein.

- [2] R. A. van Santen, H. P. C. E. Kuipers, *Adv. Catal.* **1987**, *35*, 265–321.
- [3] a) J. G. Serafin, A. C. Liu, S. R. Seyedmonir, *J. Mol. Catal. A* **1998**, *131*, 157–168; b) W. E. Evans, P. I. Chipman (Shell Oil Company), US Patent 6717001 B2, **2004**.
- [4] a) T. C. R. Rocha, A. Oestereich, D. V. Demidov, M. Hävecker, S. Zafeiratos, G. Weinberg, V. I. Bukhtiyarov, A. Knop-Gericke, R. Schlögl, *Phys. Chem. Chem. Phys.* **2012**, *14*, 4554–4564; b) T. E. Jones, T. C. R. Rocha, A. Knop-Gericke, C. Stampfl, R. Schlögl, S. Piccinin, *Phys. Chem. Chem. Phys.* **2015**, *17*, 9288–9312; c) T. E. Jones, T. C. R. Rocha, A. Knop-Gericke, C. Stampfl, R. Schlögl, S. Piccinin, *ACS Catal.* **2015**, *5*, 5846–5850; d) T. E. Jones, R. Wyrwich, S. Böcklein, E. A. Carbonio, M. T. Greiner, A. Yu. Klyushin, W. Moritz, A. Locatelli, T. O. Mentes, M. A. Niño, A. Knop-Gericke, R. Schlögl, S. Günther, J. Winterlin, S. Piccinin, *ACS Catal.* **2018**, *8*, 3844–3852; e) E. A. Carbonio, T. C. R. Rocha, A. Yu. Klyushin, I. Piš, E. Magnano, S. Nappini, S. Piccinin, A. Knop-Gericke, R. Schlögl, T. E. Jones, *Chem. Sci.* **2018**, *9*, 990–998.
- [5] a) M. Egashira, R. L. Kuczkowski, N. W. Cant, *J. Catal.* **1980**, *65*, 297–310; b) S. Linic, M. A. Barteau, *J. Am. Chem. Soc.* **2002**, *124*, 310–317; c) S. Linic, M. A. Barteau, *J. Catal.* **2003**, *214*, 200–212; d) S. Linic, M. A. Barteau, *J. Am. Chem. Soc.* **2003**, *125*, 4034–4035.
- [6] a) M. O. Özbeş, I. Onal, R. A. van Santen, *J. Catal.* **2011**, *284*, 230–235; b) M. O. Özbeş, R. A. van Santen, *Catal. Lett.* **2013**, *143*, 131–141.
- [7] a) A. Chongtertoonskul, J. W. Schwank, S. Chavadej, *J. Mol. Catal. A* **2012**, *358*, 58–66; b) A. Chongtertoonskul, J. W. Schwank, S. Chavadej, *Catal. Lett.* **2012**, *142*, 991–1002.
- [8] a) M. O. Özbeş, I. Önal, R. A. van Santen, *ChemCatChem* **2013**, *5*, 443–451; b) T. C. R. Rocha, M. Hävecker, A. Knop-Gericke, R. Schlögl, *J. Catal.* **2014**, *312*, 12–16; c) M. T. Greiner, T. C. R. Rocha, B. Johnson, A. Klyushin, A. Knop-Gericke, R. Schlögl, *Z. Phys. Chem.* **2014**, *228*, 521–541; d) W. Diao, C. DiGiulio, M. T. Schaaf, S. Ma, J. R. Monnier, *J. Catal.* **2015**, *322*, 14–23; e) D. Ren, G. Cheng, J. Li, J. Li, W. Dai, X. X. Sun, D. Cheng, *Catal. Lett.* **2017**, *147*, 2920–2928; f) M. Huš, A. Hellman, *J. Catal.* **2018**, *363*, 18–25.
- [9] J. Lu, J. J. Bravo-Suárez, A. Takahashi, M. Haruta, S. T. Oyama, *J. Catal.* **2005**, *232*, 85–95.
- [10] T. E. Jones, T. C. R. Rocha, A. Knop-Gericke, C. Stampfl, R. Schlögl, S. Piccinin, *Phys. Chem. Chem. Phys.* **2014**, *16*, 9002–9014.
- [11] T. E. Jones, R. Wyrwich, S. Böcklein, T. C. R. Rocha, E. A. Carbonio, A. Knop-Gericke, R. Schlögl, S. Günther, J. Winterlin, S. Piccinin, *J. Phys. Chem. C* **2016**, *120*, 28630–28638.
- [12] T. Suttipul, T. Sreethawong, H. Sekiguchi, S. Chavadej, *Plasma Chem. Plasma Process.* **2011**, *31*, 273–290.
- [13] J. E. van den Reijen, S. Kanungo, T. A. J. Wellings, M. Versluijs-Helder, T. A. Nijhuis, K. P. de Jong, P. E. de Jongh, *J. Catal.* **2017**, *356*, 65–74.
- [14] A. Indra, M. Greiner, A. Knop-Gericke, R. Schlögl, D. Avnir, M. Driess, *ChemCatChem* **2014**, *6*, 1935–1939.
- [15] a) D. Sun, H. Wang, G. Zhang, J. Huang, Q. Li, *RSC Adv.* **2013**, *3*, 20732–20737; b) X. Jing, H. Wang, H. Chen, J. Huang, Q. Li, D. Sun, *RSC Adv.* **2014**, *4*, 27597–27603; c) X. Jing, J. Huang, H. Wang, M. Du, D. Sun, Q. Li, *Chem. Eng. J.* **2016**, *284*, 149–157.
- [16] a) S. S. Sangaru, H. Zhu, D. C. Rosenfeld, A. K. Samal, D. Anjum, J.-M. Basset, *ACS Appl. Mater. Interfaces* **2015**, *7*, 28576–28584; b) A. Ramirez, J. L. Hueso, H. Suarez, R. Mallada, A. Ibarra, S. Irusta, J. Santamaría, *Angew. Chem. Int. Ed.* **2016**, *55*, 11158–11161; *Angew. Chem.* **2016**, *128*, 11324–11327; c) D. Kim, Y. Lee, Y. Kim, K. Mingle, J. Lauterbach, D. A. Blom, T. Vogt, Y. Lee, *Chem. Eur. J.* **2018**, *24*, 1041–1045.
- [17] S. Linic, J. Jankowiak, M. A. Barteau, *J. Catal.* **2004**, *224*, 489–493.
- [18] a) J. T. Jankowiak, M. A. Barteau, *J. Catal.* **2005**, *236*, 366–378; b) J. T. Jankowiak, M. A. Barteau, *J. Catal.* **2005**, *236*, 379–386; c) J. C. Dellamorte, J. Lauterbach, M. A. Barteau, *Catal. Today* **2007**, *120*, 182–185; d) J. C. Dellamorte, J. Lauterbach, M. A. Barteau, *Appl. Catal. A* **2011**, *391*, 281–288.
- [19] a) S. Piccinin, S. Zafeiratos, C. Stampfl, T. W. Hansen, M. Hävecker, D. Teschner, V. I. Bukhtiyarov, F. Girgsdies, A. Knop-Gericke, R. Schlögl, M. Scheffler, *Phys. Rev. Lett.* **2010**, *104*, 035503–1–4; b) S. Piccinin, N. L. Nguyen, C. Stampfl, M. Scheffler, *J. Mater. Chem.* **2010**, *20*, 10521–10527; c) N. L. Nguyen, S. Piccinin, S. de Gironcoli, *J. Phys. Chem. C* **2011**, *115*, 10073–10079; d) N. L. Nguyen, S. de Gironcoli, S. Piccinin, *J. Chem. Phys.* **2013**, *138*, 184707–1–8; e) M. T. Greiner, J. Cao, T. E. Jones, S. Beeg, K. Skopurska, E. A. Carbonio, H. Sezen, M. Amati, L. Gregoratti, M.-G. Willinger, A. Knop-Gericke, R. Schlögl, *ACS Catal.* **2018**, *8*, 2286–2295.
- [20] J. C. Dellamorte, M. A. Barteau, J. Lauterbach, *Surf. Sci.* **2009**, *603*, 1770–1775.
- [21] B. K. Bonin, X. E. Verykios, *J. Catal.* **1985**, *91*, 36–43.
- [22] N. Toreis, X. E. Verykios, S. M. Khalid, G. Bunker, Z. R. Korszun, *J. Catal.* **1988**, *109*, 143–155.
- [23] a) M. Armbrüster, K. Kovnir, M. Behrens, D. Teschner, Yu. Grin, R. Schlögl, *J. Am. Chem. Soc.* **2010**, *132*, 14745–14747; b) M. Armbrüster, K. Kovnir, M. Friedrich, D. Teschner, G. Wovsnick, M. Hahne, P. Gille, L. Szenthilki, M. Feuerbacher, M. Heggen, F. Girgsdies, D. Rosenthal, R. Schlögl, Yu. Grin, *Nat. Mater.* **2012**, *11*, 690–693; c) M. Armbrüster, R. Schlögl, Yu. Grin, *Sci. Technol. Adv. Mater.* **2014**, *15*, 034803–1–17.
- [24] M. Paní, M. L. Fornasini, F. Merlo, *Z. Kristallogr.* **2007**, *222*, 218–225.
- [25] a) N. Baar, Z. *Anorg. Allg. Chem.* **1911**, *70*, 352–394; b) W. A. Alexander, L. D. Calvert, A. Desaulniers, H. S. Dunsmore, D. F. Sargent, *Can. J. Chem.* **1969**, *47*, 611–614; c) M. R. Baren, *Bull. Alloys Phase Diagr.* **1988**, *9*, 228–229.
- [26] a) C. Stampfl, M. V. Ganduglia-Pirovano, K. Reuter, M. Scheffler, *Surf. Sci.* **2002**, *500*, 368–394; b) K. Reuter, M. Scheffler, *Appl. Phys. A* **2004**, *78*, 793–798; c) J. K. Nørskov, M. Scheffler, H. Toulhoat, *MSR Bull.* **2006**, *31*, 669–674.
- [27] N. W. Cant, W. K. Hall, *J. Catal.* **1978**, *52*, 81–94.
- [28] R. A. van Santen, J. Moolhuysen, W. M. H. Sachtler, *J. Catal.* **1980**, *65*, 478–480.
- [29] R. B. Grant, R. M. Lambert, *J. Catal.* **1985**, *92*, 364–375.
- [30] a) A. Ayame, Y. Uchida, H. Ono, M. Miyamoto, T. Sato, H. Hayasaka, *Appl. Catal. A* **2003**, *244*, 59–70; b) G. Boskovic, N. Dropka, D. Wolf, A. Brückner, M. Baerns, *J. Catal.* **2004**, *226*, 334–342; c) J. Jiang, T. Xu, Y. Li, X. Lei, H. Zhang, D. G. Evans, X. Sun, X. Duan, *Bull. Korean Chem. Soc.* **2014**, *35*, 1832–1836.
- [31] a) C. T. Campbell, M. T. Paffett, *Appl. Surf. Sci.* **1984**, *19*, 28–42; b) C. T. Campbell, *J. Catal.* **1986**, *99*, 28–38; c) S. A. Tan, R. B. Grant, R. M. Lambert, *J. Catal.* **1987**, *106*, 54–64; d) K. L. Yeung, A. Gavrilidis, A. Varma, M. M. Bhasin, *J. Catal.* **1998**, *174*, 1–12.
- [32] a) A. E. B. Presland, G. L. Price, D. L. Trimm, *J. Catal.* **1972**, *26*, 313–317; b) G. L. Montrasi, G. R. Tauszik, M. Solari, G. Leofanti, *Appl. Catal.* **1983**, *5*, 359–369; c) E. Ruckenstein, S. H. Lee, *J. Catal.* **1988**, *109*, 100–119; d) X. G. Zhou, W. K. Yuan, *Chem. Eng. Sci.* **2004**, *59*, 1723–1731; e) G. Boskovic, D. Wolf, A. Brückner, M. Baerns, *J. Catal.* **2004**, *224*, 187–196.
- [33] R. F. W. Bader, *Atoms in Molecules: A Quantum Theory*, Clarendon Press, Oxford, **1995**.
- [34] K. Reuter, M. Scheffler, *Phys. Rev. Lett.* **2003**, *90*, 046103–1–4.
- [35] M. W. Chase, *NIST-JANAF Thermochemical Tables*, National Institute of Standards and Technology, Washington, **1998**.
- [36] WinXPow (Version 2.25), STOE and Cie GmbH, Darmstadt (Germany), **2009**.
- [37] L. Akselrud, Yu. Grin, *J. Appl. Crystallogr.* **2014**, *47*, 803–805.
- [38] S. A. Schunk, D. Demuth, A. Cross, O. Gerlach, A. Haas, J. Klein, J. M. Newsam, A. Sundermann, W. Stichert, W. Strehlau, U. Vietze, T. Zech, “Chapter 2: Mastering the Challenges of Catalyst Screening in High-Throughput Experimentation for Heterogeneously Catalyzed Gas-Phase Reactions” in *High-throughput Screening in Heterogeneous Catalysis* (Eds.: A. Hagemeyer, P. Strasser, A. F. Volpe), Wiley-VCH, Weinheim, **2004**, pp. 19–62.
- [39] V. Blum, R. Gehrke, F. Hanke, P. Havu, V. Havu, X. Ren, K. Reuter, M. Scheffler, *Comput. Phys. Commun.* **2009**, *180*, 2175–2196.
- [40] J. P. Perdew, K. Burke, M. Ernzerhof, *Phys. Rev. Lett.* **1996**, *77*, 3865–3868.
- [41] E. van Lenthe, E. J. Baerends, J. G. Snijders, *J. Chem. Phys.* **1994**, *101*, 9783–9792.
- [42] M. Kohout, *Int. J. Quantum Chem.* **2004**, *97*, 651–658.
- [43] a) M. Kohout, F. R. Wagner, Yu. Grin, *Int. J. Quantum Chem.* **2006**, *106*, 1499–1507; b) M. Kohout, *Faraday Discuss.* **2007**, *135*, 43–54.
- [44] S. A. Villaseca, A. Ormeci, S. V. Levchenko, R. Schlögl, Yu. Grin, M. Armbrüster, *ChemPhysChem* **2017**, *18*, 334–337.
- [45] M. Kohout, *Program DGRID*, version 4.6, Radebeul (Germany), **2011**.

Received: June 5, 2018